Electronic Supplementary Material (ESI) for Physical Chemistry Chemical Physics.
This journal is © the Owner Societies 2022

Electronic Supporting Information

Theoretical seeking of the charge transport materials with inherent mobility higher than 2,6-Diphenyl anthracene: three isomers of 2,6-Dipyridyl anthracene

Guiya Qin,[a] Panpan Lin,[a,c] Xiaoqi Sun,[b] Jingfu Guo,*[b] Jianxun Fan, [d] Lifei J i,[e] Hui Li,[a] and Aimin Ren*[a]

[a.] *Institute of Theoretical Chemistry, College of Chemistry, Jilin University, Changchun, 130023, China.*

[b.] *School of Physics, Northeast Normal University, Changchun 130024, P.R. China.*

[c.] *College of Chemistry and Chemical Engineering, Qiqihar University, Qiqihar, 161006, P.R. China.*

[d.] *College of Chemistry and Materials Science, Weinan Normal University, Weinan,714000, China.*

[e.] *Hebei Provincial Key Laboratory of Photoelectric Control on Surface and Interface, Hebei University of Science and Technology, Shijiazhuang, 050018, P.R. China.*

*E-mail: aimin_ren@yahoo.com; renam@jlu.edu.cn

CONTENTS

Table S1 The torsion angles between substituent moieties and anthracene core plane

Table S2 The frontier molecular orbital and energy gap of theoretical calculation and experimental data.

Table S3 The values of λ_h in different frequency ranges.

Table S4 The average values of transfer integrals |<V>| and the corresponding standard deviations σ from thermal fluctuation for 2,6-DPA.

Table S5 The charge transfer rate (k_{CT}) for each transport pathway.

Table S6 The range of anisotropic μ_h for the condition of static state and thermal fluctuation.

Table S7 Morphology predictions for three 2,6-DPyAs and 2,6-DPA.

Fig. 1 The Hirshfeld surface with shape index for **2,6-DPA.**

Fig. 2 The topological properties at the intermolecular N···H BCPs (bond critical points).

Fig. S3. The herringbone angels, displacements along long-axis/short-axis and the face-to-face distances between the most nearest-neighboring π-stacking dimers.

Fig. S4 The V_hs of 1800 snapshots along herringbone packing direction of 2,6-DPA (dimer 1) at different temperatures.

Fig. S5 The V_hs of 1800 snapshots along the main transport pathways of herringbone packing direction (dimer 1) of **2,6-DPyA.**

Fig. S6-S8 Count distributions of the transfer integral V of the uppermost transport pathways for 2,6-DPyAs at 300K, 200K, and 100K.

Fig. S9 The curves of the reference transfer rate (k_{CT}) with temperature changes.

Fig. S10-13 The respective outcropping atoms on the plane of relative Miller indices for 2,6-DPA and 2,6-DPyAs.

Noting: The crystallographic data of 2,6-DPA, 2,6-DPyA-a, 2,6-DPyA-b, 2,6-DPyA-c are obtained by the Hu group.[1-2]

Table S1. The torsion angles between substituent moieties and anthracene core plane of studied molecules for both obtained by QM/MM method (B3LYP/6-31+G(d, p)/UFF) and directly measured in crystals.

	QM/MM		Crystal		Gas	
	Dihedral angle 1	Dihedral angle 2	Dihedral angle 1	Dihedral angle 2	Dihedral angle 1	Dihedral angle 2
2,6-DPyA-a	26.19	-26.21	30.64	-30.64	21.42	-21.42
2,6-DPyA-b	34.20	-33.13	33.62	-33.50	39.68	-39.65
2,6-DPyA-c	9.34	-9.35	-5.36	5.36	-37.80	37.90
2,6-DPA	19.53	-19.55	20.05	-20.05	37.43	-37.46

Table S2. The frontier molecular orbital and energy gap of theoretical calculation (QM/MM, B3LYP/6-31+G(d, p)/UFF) and experimental data.

	QM/MM				Experimental data			
	HOMO	LUMO	Gap	Optical Gap	HOMO	LUMO	Gap	Optical Gap
2,6-DPyA-a	-5.45	-2.18	3.27	2.93	-5.37[b]	--	--	2.95
2,6-DPyA-b	-5.68	-2.35	3.32	3.00	-5.58[b]	--	--	3.01
2,6-DPyA-c	-5.84	-2.63	3.21	2.89	-5.90[b]	--	--	2.95
2,6-DPA	-5.41 (-5.38[a])	-2.16 (-1.76[a])	3.25 (3.68[a])	2.92	-5.60[c]	-2.60	3.00	--

a: the theoretical calculation results by PBE0/6-31G(d) level.

b: the measured results by ultraviolet photoelectron spectrometry in thin film.

c: obtained by cyclic-voltammetry of 2,6-DPA.

Table S3. The values of hole reorganization energies (λ_h) in different frequency ranges. (in cm^{-1})

Compd. \ Freq.	0~500	500~1250	1250~1700	1700~	λ_h (total)
2,6-DPyA-a	11.33	8.92	107.92	0.31	128.48
2,6-DPyA-b	22.56	12.77	108.31	0.32	143.96
2,6-DPyA-c	10.70	13.09	109.18	0.28	133.25
2,6-DPA	23.85	14.65	103.44	0.35	142.29

Table S4. The average values of transfer integrals $|<V>|$ and the corresponding standard deviations σ from thermal fluctuation at 300 K, 250K, 200K, 150K and 100K for **2,6-DPA.** (V_{static} represents for the static transport integral) (Unit: meV)

	Dimer 1 ($V_{\text{static}} = 56.97$)			Dimer 3 ($V_{\text{static}} = 10.13$)		
	$\|<V>\|$	σ	$\sigma/\|<V>\|$	$\|<V>\|$	σ	$\sigma/\|<V>\|$
300K	39.67	23.99	0.60	6.77	7.72	1.14
250K	41.60	21.31	0.51	5.08	6.41	1.26
200K	45.28	19.72	0.44	5.42	6.10	1.13
150K	46.16	17.19	0.37	5.74	5.93	1.03
100K	47.44	10.65	0.22	6.60	3.40	0.52

Table S5. The charge-transfer rate (k_{CT}) based on the full quantum nuclear tunneling model for each transport pathway at 300K.(Unit: s^{-1})

	$k_{\text{CT}}\times10^{12}$		
	dimer1	dimer2	dimer3
2,6-DPyA-a	162.0	162.0	25.13

2,6-DPyA-b	249.0	236.4	54.61
2,6-DPyA-c	2.580	2.583	2.548
2,6-DPA	175.1	175.1	5.538

Table S6. The range of anisotropic μ_h for the condition of static state and thermal fluctuation at 300K, 200K and 100K.(Unit: cm^2 V^{-1} s^{-1})

	μ_h			
	static	300K	200K	100K
2,6-DPyA-a	7.91~8.40	1.92~2.16	5.99~7.18	11.94~13.89
2,6-DPyA-b	12.73~13.34	8.93~9.24	18.59~18.83	43.60~49.35
2,6-DPyA-c	0.27~0.30	0.18~0.53	0.18~0.90	0.14~2.31
2,6-DPA	7.01~9.13	3.54~4.71	8.11~11.03	29.86~39.97

Table S7. Morphology predictions for three **2,6-DPyA**s and **2,6-DPA** molecules by means of AE calculations.

2,6-DPA

{hkl}	Multiplicity	d_{hkl}(Å)[b]	% of Total Facet Area[c]	Total Attachment Energy[d]	Eatt (vdW)	Eatt (electrostatic)	r[e]
{100}	2	17.972	71.516	-9.027	-8.181	-0.846	1
{110}	4	6.804	11.717	-39.595	-34.107	-5.488	4.386
{011}	4	4.759	16.767	-52.974	-44.342	-8.633	5.868

2,6-DPyA-a

{hkl}	Multiplicity	d_{hkl}(Å)[b]	%of Total Facet Area[c]	Total Attachment Energy[d]	Eatt (vdW)	Eatt (electrostatic)	r[e]
{100}	2	17.196	72.522	-9.331	-6.790	-2.541	1
{110}	4	5.861	4.501	-51.935	-42.423	-9.513	5.57

{011}	4	4.738	8.821	-50.090	-43.171	-6.919	5.37
{11-1}	4	4.661	8.631	-49.317	-41.996	-7.321	5.285
{10-2}	2	3.655	5.525	-55.604	-52.716	-2.888	5.959

2,6-DPyA-b

{hkl}	Multiplicity	d_{hkl}(Å) [b]	%of Total Facet Area [c]	Total Attachment Energy[d]	Eatt (vdW)	Eatt (electrostatic)	r [e]
{002}	1	17.515	39.718	-13.623	-10.767	-2.856	1
{00-2}	1	17.515	39.718	-13.623	-10.767	-2.856	1
{010}	2	6.280	5.152	-98.605	-75.876	-22.729	7.238
{110}	4	4.798	6.938	-104.474	-82.863	-21.612	7.669
{111}	4	4.754	2.282	-104.630	-84.111	-20.519	7.680
{11-1}	4	4.754	2.282	-104.630	-84.111	-20.519	7.680
{200}	2	3.718	3.911	-121.305	-106.679	-14.626	7.83

2,6-DPyA-c

{hkl}	Multiplicity	d_{hkl}(Å) [b]	%of Total Facet Area [c]	Total Attachment Energy[d]	E_{att} (vdW)	E_{att} (electrostatic)	r [e]
{100}	2	12.244	74.308	-8.847	-10.932	2.085	1
{110}	4	5.386	2.289	-52.490	-44.605	-7.885	5.933
{011}	4	5.218	4.207	-54.797	-48.601	-8.196	6.194
{11-1}	4	5.010	12.116	-51.053	-40.014	-11.039	5.771
{20-2}	2	4.557	2.622	-54.577	-42.317	-12.260	6.169
{10-4}	2	2.720	0.447	-63.423	-53.249	-10.174	7.169
{10-6}	2	1.807	0.307	-63.423	-53.249	-10.174	7.169
{10-8}	2	1.347	0.343	-63.423	-53.249	-10.174	7.169
{30-10}	2	1.088	0.226	-63.423	-53.249	-10.174	7.169
{20-10}	2	1.086	0.446	-63.423	-53.249	-10.174	7.169
{40-14}	2	0.777	0.283	-63.423	-53.249	-10.174	7.169

{20-14}	2	0.773	0.314	-63.423	-53.249	-10.174	7.169
{40-18}	2	0.604	0.336	-63.423	-53.248	-10.174	7.169
{20-18}	2	0.599	0.224	-63.423	-53.248	-10.174	7.169
{60-22}	2	0.495	0.375	-63.423	-53.249	-10.174	7.169
{40-22}	2	0.493	0.367	-63.423	-53.249	-10.174	7.169
{60-26}	2	0.418	0.300	-63.423	-53.249	-10.174	7.169
{80-26}	2	0.418	0.227	-63.423	-53.249	-10.174	7.169
{40-26}	2	0.416	0.260	-63.423	-53.249	-10.174	7.169

[a]: All energies are in kcal/mol, distance is in Å, and area in Å^2.

[b]: Interplanar distance.

[c]: The percentage of the total growth face areas occupied by all symmetry images of the facet.

[d]: Total Attachment Energy = E_{att} (vdW)+ E_{att} (electrostatic).

[e]: The growth rate of (hkl) facet , which is proportional to the attachment energy of the crystal.

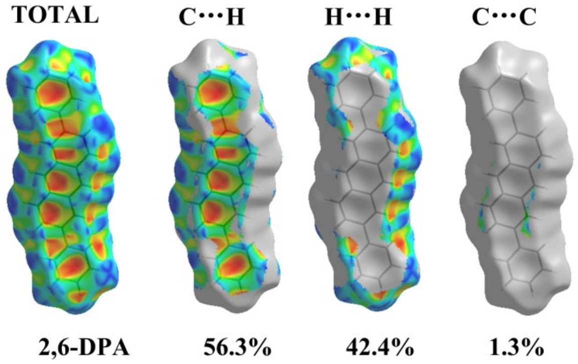

Fig. S1. The Hirshfeld surface with shape index for **2,6-DPA**.

(The analysis methods for Hirshfeld surface

It is widely known that organic molecules are combined together through noncovalent interactions, as a result, to better understand the molecular packing−property relationships, the intermolecular interactions in these crystals were investigated. Molecular Hirshfeld surfaces are constructed by partitioning space in the crystal into regions where the electron distribution of a sum of spherical atoms for the molecule dominates the corresponding sum over the crystal. [3] It is always used to visualize and analyze weak intermolecular interactions, due to its convenience and usefulness. The normalized contact distance (d_{norm}) enables identifying the regions of particular important intermolecular contacts, and defined as:

$$d_{norm} = \frac{d_i - r_i^{vdW}}{r_i^{vdW}} + \frac{d_e - r_e^{vdW}}{r_e^{vdW}} \qquad (1)$$

Where r^{vdW} is the atomic van der Waals radius, d_e and d_i are the distances from the Hirshfeld surface to the nearest atoms outside and inside the surface, respectively. In order to capture the intuitive notion of 'local shape' well, the shape index (SI) is chosen to map on Hirshfeld surfaces in this work, defined as:[4]

$$S = \frac{2}{\pi} arctan\left(\frac{\kappa_1 + \kappa_2}{\kappa_1 - \kappa_2}\right) \qquad (2)$$

Here, κ_1 and κ_2 are principal curvatures. **)**

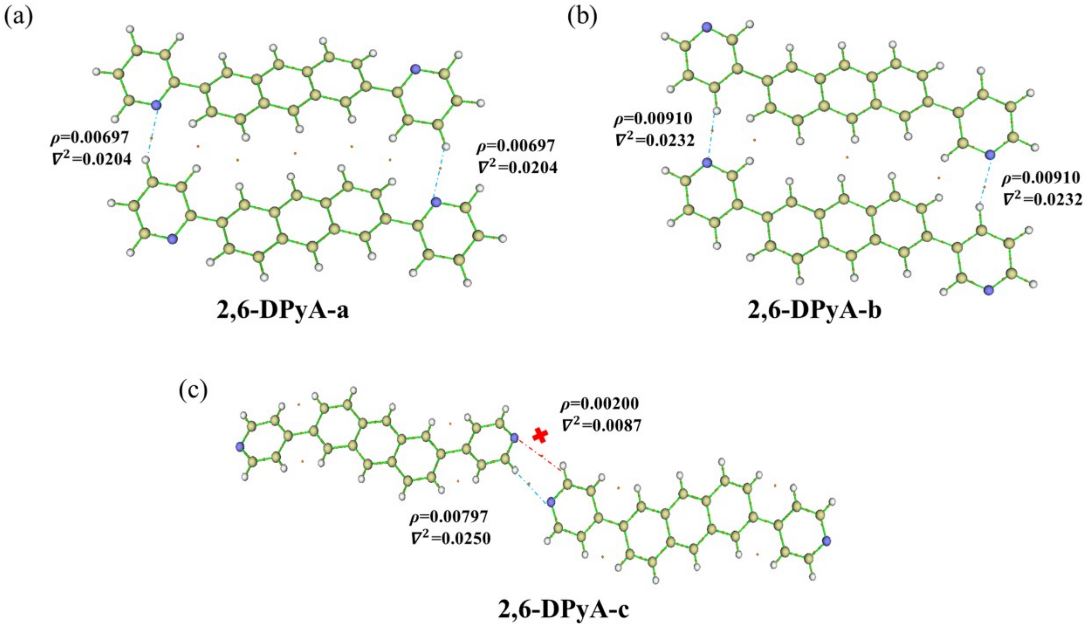

Fig. S2. The topological properties at the intermolecular N⋯H BCPs (bond critical points)[5] calculated at the B3LYP/cc-pVDZ level. (Generally, the values of electronic density and laplacian at BCP of H-bond are in the range of [0.002,0.04] and [0.02,0.15], respectively.[6])

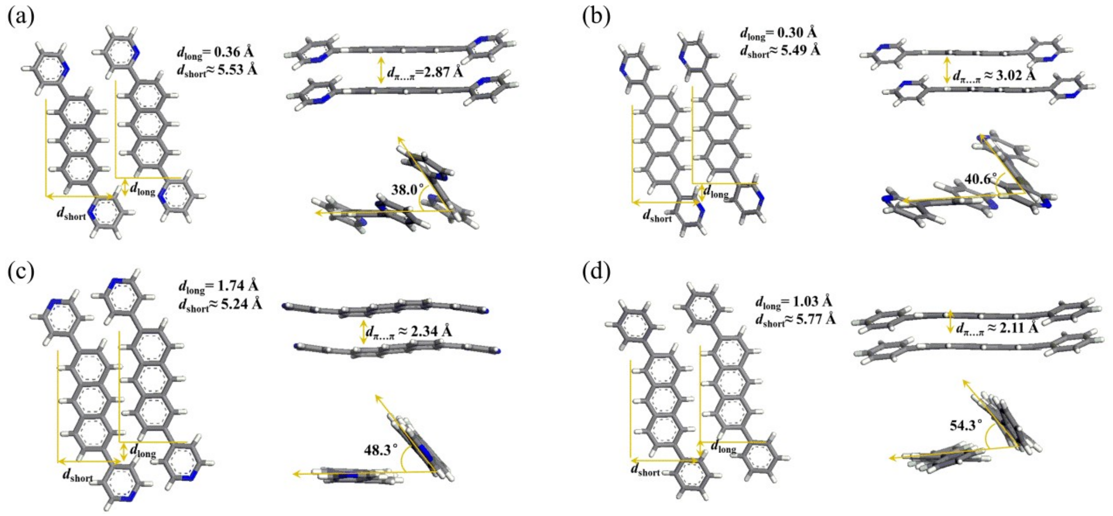

Fig. S3. The herringbone angels, displacements along long-axis/short-axis and the face-to-face distances of the most nearest-neighboring π-stacking dimers. (a), (b), (c) and (d) refers to **2,6-DPyA-a**, **2,6-DPyA-b**, **2,6-DPyA-c** and **2,6-DPA**, respectively.

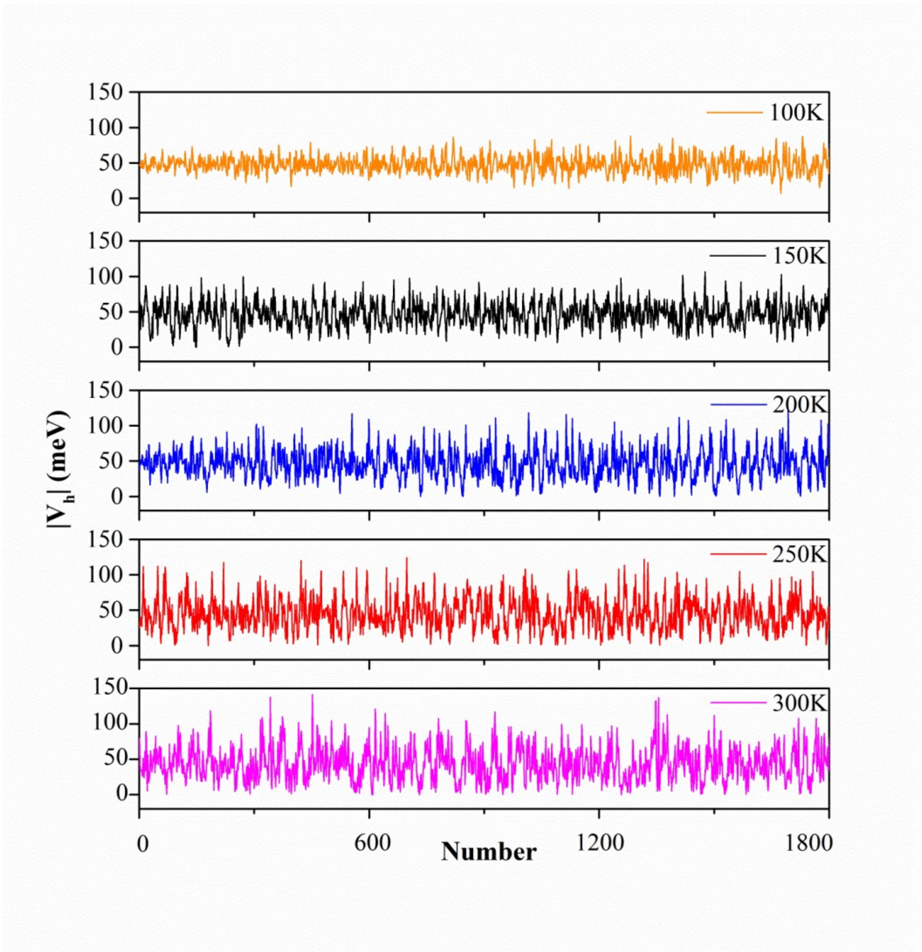

Fig. S4. The V_hs of 1800 snapshots along the main transport pathways of herringbone packing direction of **2,6-DPA** (dimer 1) at different temperatures.

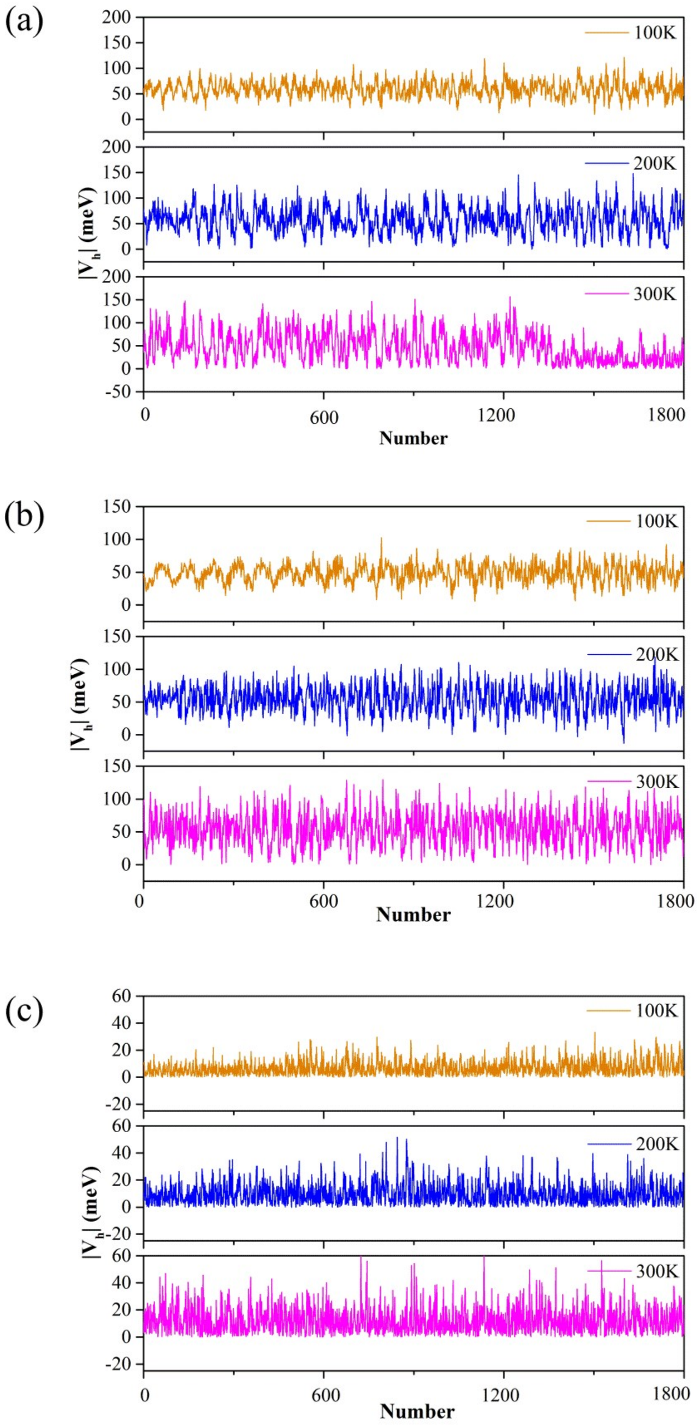

Fig. S5. The V_hs of 1800 snapshots along the main transport pathways of herringbone packing direction (dimer 1) of **2,6-DPyA-a**, （a）, **2,6-DPyA-b**, (b), and **2,6-DPyA-c**, (c) at different temperatures.

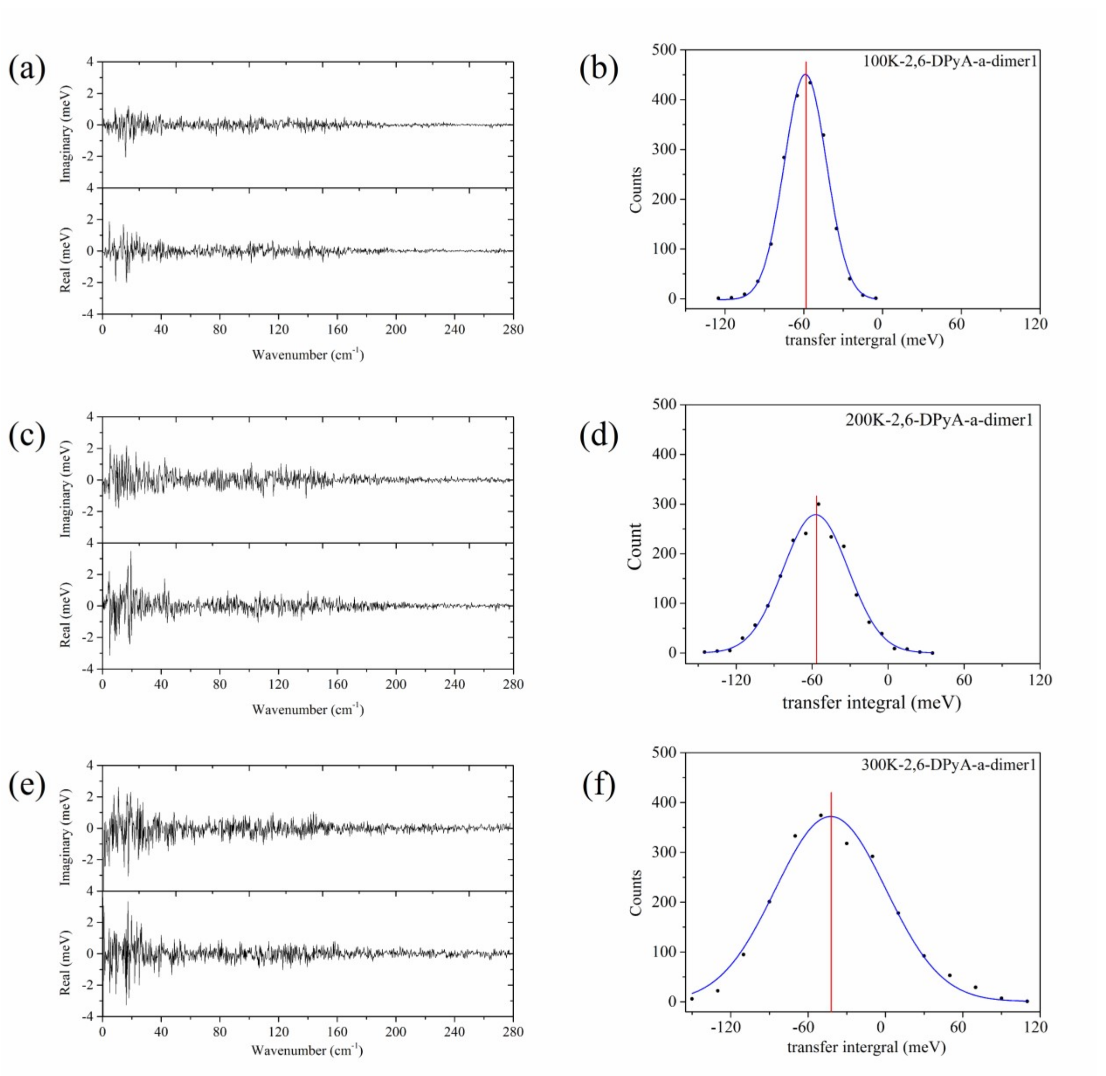

Fig. S6. Count distributions of the transfer integral V of the uppermost transport pathways for 2,6-DPyA-a at 300K, 200K, and 100K on the right side. In (b), (d) and (f), the blue solid line represents the Gaussian fit, the red vertical line points to the average values of transfer integrals $\langle V \rangle$. (a), (c) and (e) represent the Fourier transformations of thermal deviation amplitudes (real and imaginary) at corresponding temperature.

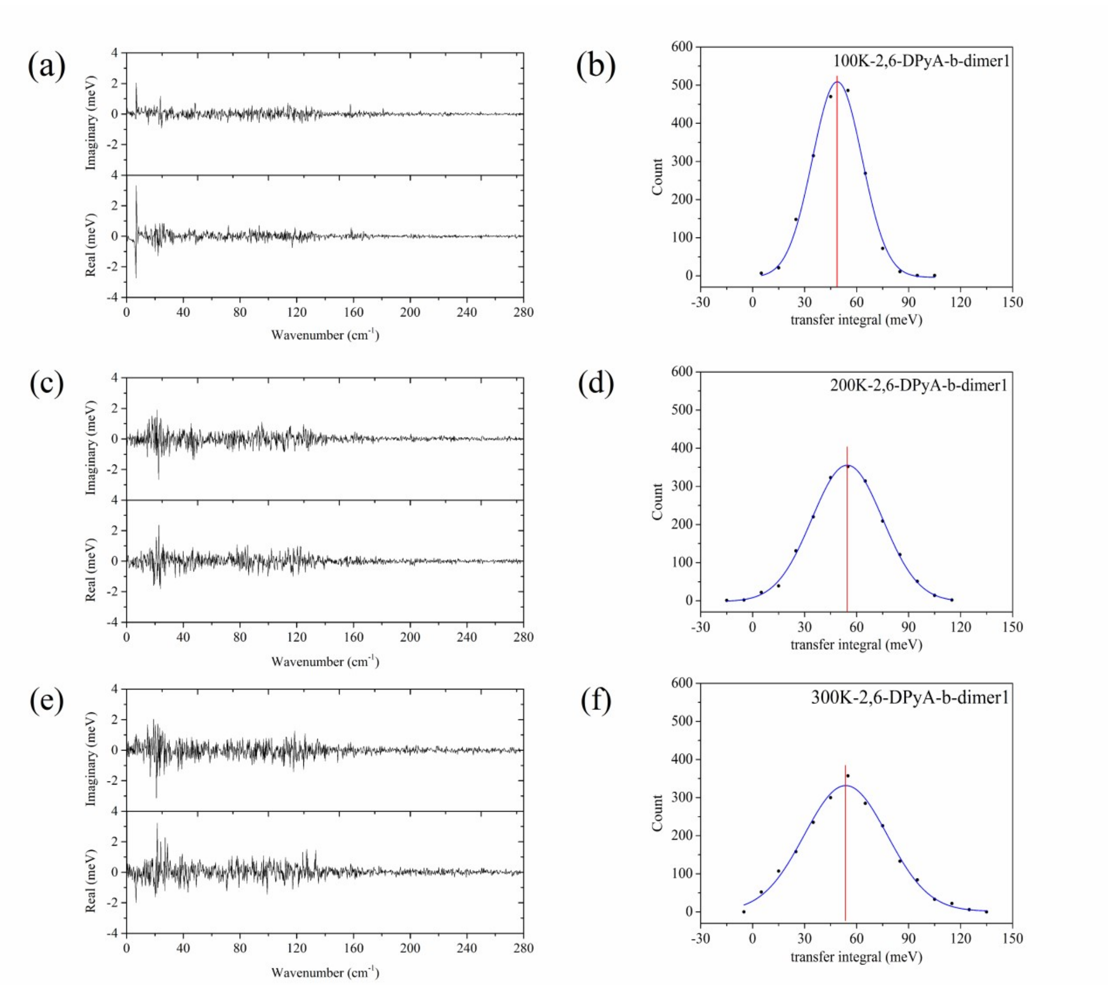

Fig. S7. Count distributions of the transfer integral V of the uppermost transport pathways for 2,6-DPyA-b at 300K, 200K, and 100K on the right side. In (b), (d) and (f), the blue solid line represents the Gaussian fit, the red vertical line points to the average values of transfer integrals $\langle V \rangle$. (a), (c) and (e) represent the Fourier transformations of thermal deviation amplitudes (real and imaginary) at corresponding temperature.

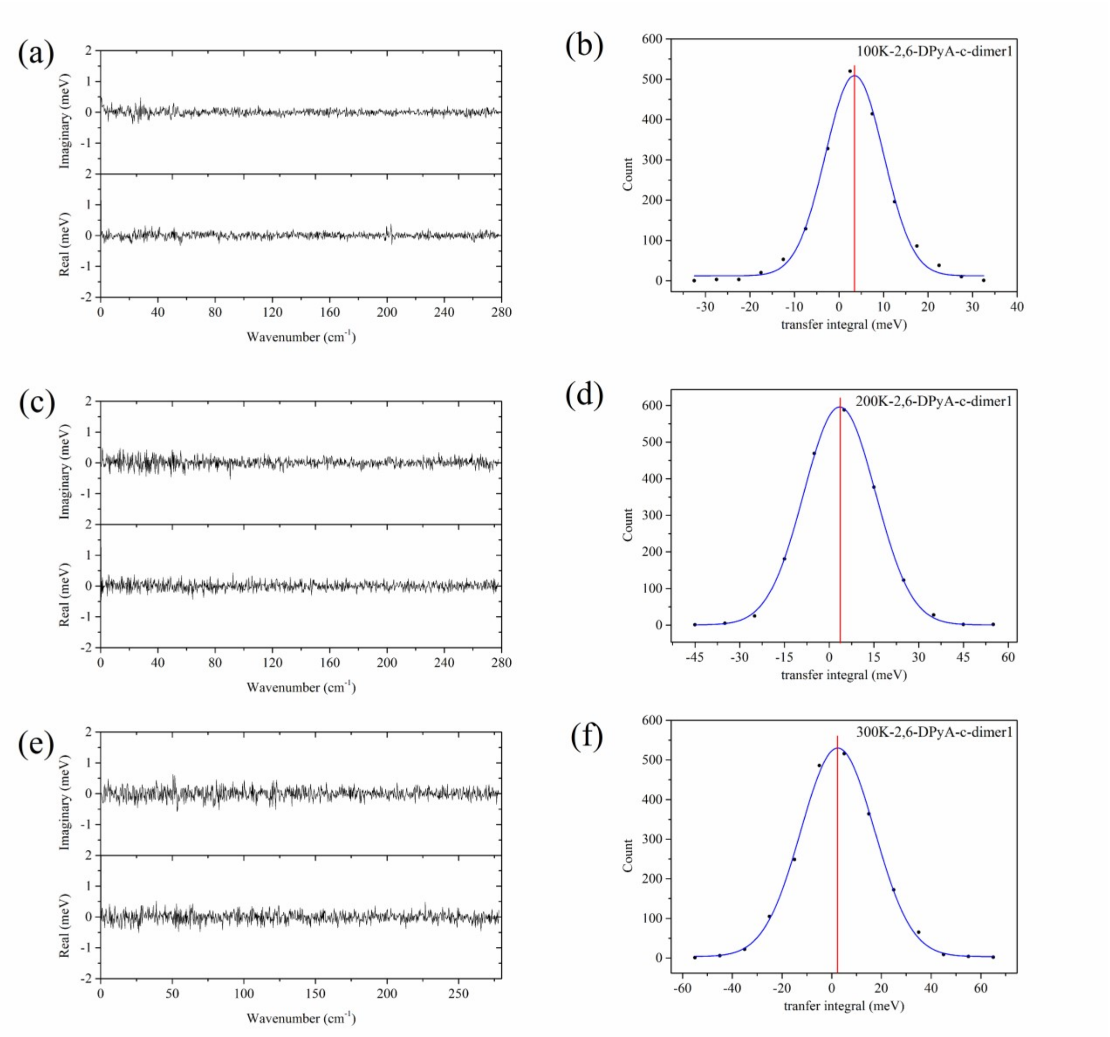

Fig. S8. Count distributions of the transfer integral V of the uppermost transport pathways for 2,6-DPyA-c at 300K, 200K, and 100K on the right side. In (b), (d) and (f), the blue solid line represents the Gaussian fit, the red vertical line points to the average values of transfer integrals $\langle V \rangle$. (a), (c) and (e) represent the Fourier transformations of thermal deviation amplitudes (real and imaginary) at corresponding temperature.

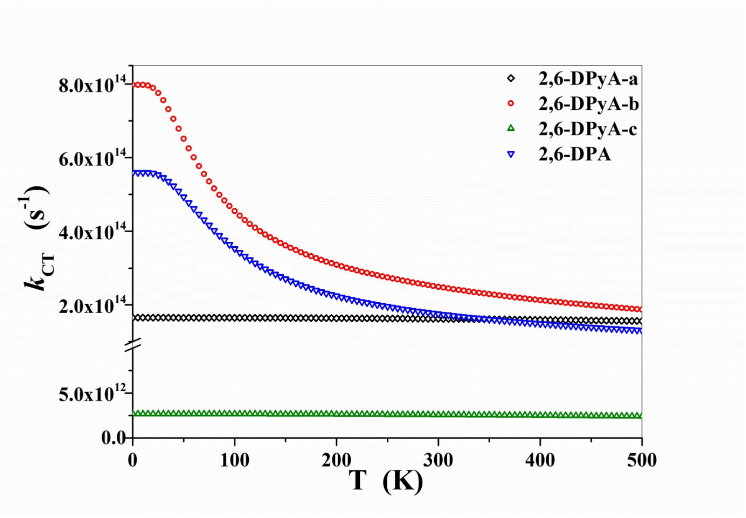

Fig. S9. The curves of the reference transfer rate (k_{CT}) with temperature changes (V=1 eV).

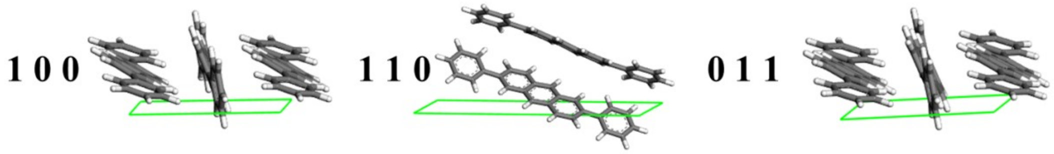

Fig. S10. The relative Miller indices of **2,6-DPA** are shown together with the respective outcropping atoms.

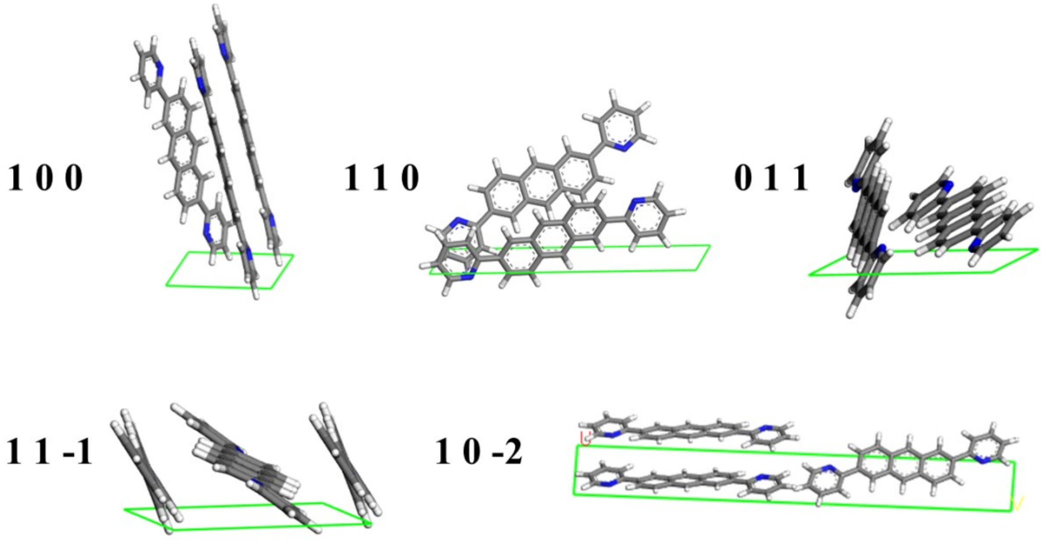

Fig. S11. The relative Miller indices of **2,6-DPyA-a** are shown together with the respective outcropping atoms.

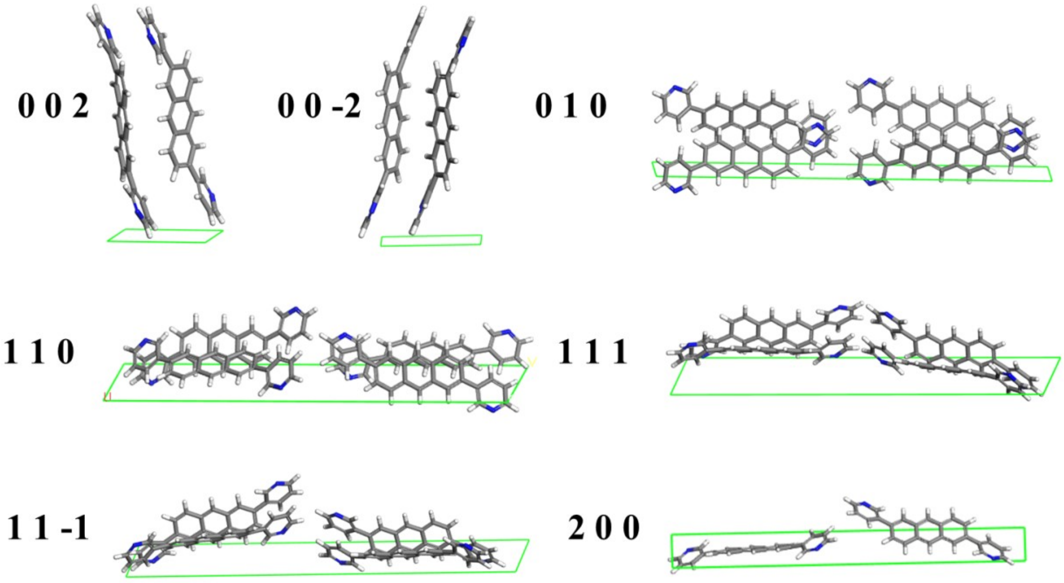

Fig. S12. The relative Miller indices of **2,6-DPyA-b** are shown together with the respective outcropping atoms.

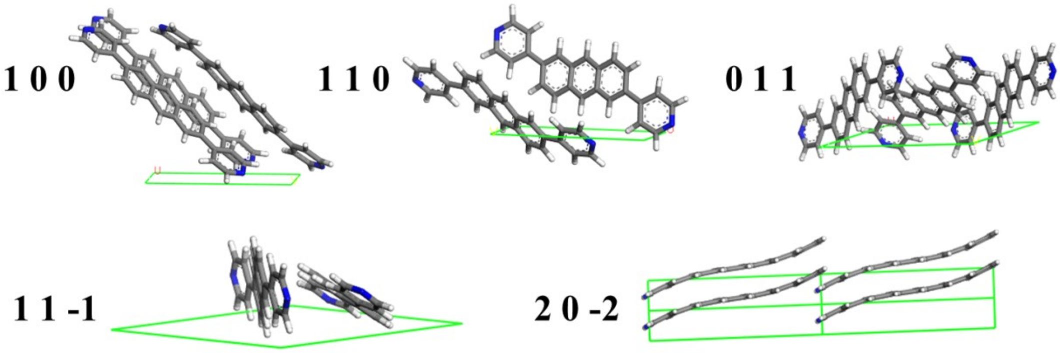

Fig. S13. The relative Miller indices of **2,6-DPyA-c** are shown together with the respective outcropping atoms.

References

1. Jie Liu, Huanli Dong, Zongrui Wang, Deyang Ji, Changli Cheng, Hua Geng, Hantang Zhang, Yonggang Zhen, Lang Jiang, Hongbing Fu, Zhishan Bo, Wei Chen, Zhigang Shuai, Wenping Hu, *Chemical Communications*, 2015, **51**, 11777-11779.
2. Jie Liu, Weigang Zhu, Ke Zhou, Zongrui Wang, Ye Zou, Qing Meng, Jie Li, Yonggang Zhen, Wenping Hu, *Journal of Materials Chemistry C*, 2016, **4**, 3621-3627.
3. J. J. McKinnon, D. Jayatilaka and M. A. Spackman, *Chemical Communications*, 2007, 3814-3816.
4. J. J. McKinnon, M. A. Spackman and A. S. Mitchell, *Acta Crystallographica Section B: Structural Science*, 2004, **60**, 627-668.
5. T. Lu and F. Chen, *Journal of Computational Chemistry*, 2012, 33, 580-592.
6. P. Lipkowski, S. J. Grabowski, T. L. Robinson and J. Leszczynski, *The Journal of Physical Chemistry A,* 2004, **108**, 10865-10872.